Journal of Nuclear Materials 464 (2015) 61–68

Contents lists available at ScienceDirect

Journal of Nuclear Materials

journal homepage: www.elsevier.com/locate/jnucmat

Processing and microstructure characterisation of oxide dispersion strengthened Fe–14Cr–0.4Ti–0.25Y_2O_3 ferritic steels fabricated by spark plasma sintering

Hongtao Zhang [a,b,*], Yina Huang [a], Huanpo Ning [c,d], Ceri A. Williams [a], Andrew J. London [a], Karl Dawson [e], Zuliang Hong [a], Michael J. Gorley [a,f], Chris R.M. Grovenor [a], Gordon J. Tatlock [e], Steve G. Roberts [a,f], Michael J. Reece [c,d], Haixue Yan [c,d], Patrick S. Grant [a]

[a] Department of Materials, University of Oxford, Parks Road, Oxford OX1 3PH, UK
[b] Department of Materials, Loughborough University, Leicester LE11 3TU, UK
[c] School of Engineering and Materials Science, Queen Mary University of London, London E1 4NS, UK
[d] Nanoforce Technology Ltd, London E1 4NS, UK
[e] Centre for Materials and Structures, University of Liverpool, Liverpool L69 3GH, UK
[f] Culham Centre for Fusion Energy, Culham Science Centre, Abingdon OX14 3DB, UK

HIGHLIGHTS

- Nanostructured ODS steels were successfully produced by SPS.
- Presence of $Y_2Ti_2O_7$ nanoclusters was confirmed by synchrotron XRD and microscopy.
- The chemistry of nanoclusters tested by ATP indicated they are Y–Ti–O oxides.

ARTICLE INFO

Article history:
Received 20 October 2014
Accepted 18 April 2015
Available online 24 April 2015

ABSTRACT

Ferritic steels strengthened with Ti–Y–O nanoclusters are leading candidates for fission and fusion reactor components. A Fe–14Cr–0.4Ti + 0.25Y_2O_3 (14YT) alloy was fabricated by mechanical alloying and subsequently consolidated by spark plasma sintering (SPS). The densification of the 14YT alloys significantly improved with an increase in the sintering temperature. Scanning electron microscopy and electron backscatter diffraction revealed that 14YT SPS-sintered at 1150 °C under 50 MPa for 5 min had a high density (99.6%), a random grain orientation and a bimodal grain size distribution (<500 nm and 1–20 μm). Synchrotron X-ray diffraction patterns showed bcc ferrite, $Y_2Ti_2O_7$, FeO, and chromium carbides, while transmission electron microscopy and atom probe tomography showed uniformly dispersed $Y_2Ti_2O_7$ nanoclusters of <5 nm diameter and number density of 1.04×10^{23} m^{-3}. Due to the very much shorter consolidation times and lower pressures used in SPS compared with the more usual hot isostatic pressing routes, SPS is shown to be a cost-effective technique for oxide dispersion strengthened (ODS) alloy manufacturing with microstructural features consistent with the best-performing ODS alloys.

1. Introduction

The increasing global demand for energy coupled with a need to reduce carbon dioxide and other emissions associated with fossil fuels has revived interest in new-build nuclear energy generation. The cost-efficient and safe utilisation of nuclear power is increasingly recognised to depend upon the availability of improved neutron resistant materials for use in next generation fission and the first fusion power plants. Reduced activation oxide dispersion strengthened (ODS) ferritic steels are amongst the most promising candidates for large scale structural materials in these plants because of their relatively stable high temperature mechanical properties and comparatively good resistance to neutron irradiation. The superior performance of ODS alloys over their conventional equivalents is attributed to the high number density of nano-sized oxide dispersoids that act as (i) pinning points to dislocation movement, (ii) nucleation sites for many small helium bubbles rather than a smaller number of more damaging large

* Corresponding author at: Department of Materials, Loughborough University, Leicester LE11 3TU, UK. Tel.: +44 1509223541; fax: +44 1509223949.
E-mail address: h.zhang3@lboro.ac.uk (H. Zhang).

http://dx.doi.org/10.1016/j.jnucmat.2015.04.029
0022-3115/

bubbles that would otherwise form, and (iii) stable sinks for irradiation induced defects such as vacancies and interstitial atoms, even at a very low volume fraction (<1 vol%) [1].

The ferritic steel matrix in these alloys is most commonly based on Fe–Cr with more than 12.7 wt% Cr. This base composition has a low susceptibility to transmutation under neutron irradiation, and avoids the presence of fcc austenite [1]. Ukai et al. first recognised the important role that Ti can play in these alloys in refining the scale of the Y_2O_3-like dispersoids [2], attributing this to precipitation reactions on heat treatment of heavily milled powder that leads to the initial formation of finer Y_2TiO_5 in preference to Y_2O_3. The relatively recent confirmation of very fine nanoclusters (NCs) of 2–5 nm diameter in mechanically alloyed and heat treated ferritic alloys containing Ti using transmission electron microscopy (TEM) [3,4] and atom probe tomography (APT) [5,6] has opened a new area of study of ODS steels for nuclear applications, since finer NC dispersoid sizes give an increase in NC number density for an equivalent volume fraction of oxide-forming addition. The TEM and APT examinations on the crystal structure and chemistry have shown that these ultra-fine NCs are enriched in Y, Ti, and O atoms, and can be uniformly distributed with an extraordinarily high number density (1.4×10^{24} m^{-3}) in nanostructured ferritic alloys [7,8]. Further, the NCs are remarkably stable at high temperatures, with negligible coarsening or reduction in number density even after isothermal aging at 1300 °C for 24 h [9]. This high number density of NCs is extremely effective in minimising the effects of neutron irradiation on the mechanical performances of ODS steels and extending possible service life [10,11].

ODS steels are usually produced by powder metallurgy routes involving mechanical alloying (MA) of Y_2O_3 and pre-alloyed or elemental metallic powders, followed by consolidation techniques, such as hot isostatic pressing (HIP) or hot extrusion. A typical composition of ferritic ODS steels is Fe–14Cr–3W–0.4Ti–0.25Y_2O_3 (wt%) [1]. There are some enduring uncertainties regarding the specific mechanism(s) of NC formation. Various possible routes have been proposed, which include:

(i) a supersaturated solid solution containing Y, Ti and O is produced by room temperature MA that decomposes and re-precipitates as NCs during high temperature consolidation [12];
(ii) MA simply fragments Y_2O_3 to such a fine scale that to most characterisation techniques it appears "dissolved" and precipitation is more akin to coarsening to a scale where Y_2O_3 can again be resolved [13], and
(iii) the Y_2O_3 becomes amorphous during MA and the subsequent precipitation is better described as (re-)crystallization [14].

All these mechanisms are supported by some experimental evidence, and one may predominate under certain conditions or certain alloys, or all may operate but to differing extents. Despite these uncertainties, MA followed by HIP to full density is the most well-established route to manufacture ODS alloys reported in the literature. However, very high pressures (200 MPa) and long soak times (4 h) during HIP are normally required to achieve high density, bulk ODS alloys [15,16], which can result in excessive grain coarsening and a high manufacturing cost. Thus, more cost-effective processes for the manufacture of ODS steels are under exploration, in particular those that offer the potential for scale-up beyond the laboratory scale.

Spark plasma sintering (SPS) is a relatively new sintering-based technique [17] in which the powder to be consolidated is loaded into an electrically and thermally conductive graphite mould and a large DC pulsed current (1000–5000 A) is applied under a uniaxial pressure. When current passes through the graphite mould (and the powder if it is electrically conductive), the powder is heated both from the outside (the mould acts as a heating element) and inside (due to Joule heating from the intrinsic electrical resistance of the powder material). SPS is characterised by very fast heating (up to 2000 °C/min) and cooling rates and short holding times (minutes) to achieve near theoretical density [17]. Thus SPS occupies a very different time–temperature–density space in powder consolidation maps when compared with conventional methods, such as hot pressing sintering and HIP with ramp rate of 50–80 °C/min and a few hours holding time. Although SPS has been studied for a rapidly growing number of materials [17], there are only a small number of studies on the fabrication and microstructural characterisation of ODS steels processed by SPS, briefly reviewed below.

Balázsi et al. [18] fabricated austenitic Fe–17Cr–12Ni–2.5Mo–2.3Si–0.1C (all weight %) and martensitic Fe–16Cr–2Ni–0.2C based ODS steels by MA and SPS with particular attention to the effect of wet and dry milling on the grain size and bending strength of consolidated ODS steels, but the microstructures of nanoprecipitates were not reported and thus the effect of processing on the formation of nanoprecipitates was yet to be clarified. Karak et al. [19] reported that ferritic ODS steel with compositions of Fe–13.5Cr–2.0Al–0.5Ti + 1.0Y_2O_3, Fe–17.5Cr–2.0Al–0.5Ti + 1.0Y_2O_3, Fe–21.5Cr–2.0Al–0.5Ti + 1.0Y_2O_3 and Fe–25.5Cr–2.0Al–0.5Ti + 1.0Y_2O_3 produced by MA and SPS exhibited 1.5–2 times greater compressive strength and improved ductility than those produced by hot press sintering and HIP, which was ascribed to the presence of 10–20 nm $Y_2Ti_2O_7$ or Y_2O_3 nano-particles observed by TEM. Sun [20,21], Xia [22] and Gao et al. [23] fabricated Fe–14Cr–3W–0.2Ti + 0.3Y, Fe–16Cr–3W–0.2Ti + 0.4Y_2O_3, Fe–9Cr–1.5W–0.45Mn–0.1Ta–0.2V–0.01Si–0.2Ti–0.1/0.2C + 0.3Y_2O_3, Fe–16Cr–5Al–3W–0.2Ti + 0.4Y_2O_3 and Fe–16Cr–2W–0.5Ti–4Al–1Zr–0.4Y_2O_3 by a sol–gel method combined with hydrogen reduction, MA and SPS techniques. They found by TEM analysis that $Y_2Ti_2O_7$ nanoprecipitates with an average size of 55 nm and number density of 3.2×10^{19} m^{-3} in Fe–14Cr–3W–0.2Ti + 0.3Y; 10–30 nm $Y_2Ti_2O_7$ nanoprecipitates in Fe–16Cr–3W–0.2Ti + 0.4Y_2O_3; a mixture of 14–20 nm Y_2O_3 and $Y_2Ti_2O_7$ clusters with number density of 5.7–8.1×10^{20} m^{-3} in Fe–9Cr–1.5W–0.45Mn–0.1Ta–0.2V–0.01Si–0.2Ti–0.1/0.2C + 0.3Y_2O_3; 20–100 nm Y–Al–O nanoprecipitates in Fe–16Cr–5Al–3W–0.2Ti + 0.4Y_2O_3, and 25 nm Y–Zr–O nanoprecipitates with number density of 2.6×10^{21} m^{-3} in Fe–16Cr–2W–0.5Ti–4Al–1Zr–0.4Y_2O_3. Both the stoichiometry and the size of these nanoprecipitates are dependent on the alloy chemistry and SPS conditions. The above results may suggest that NCs in ODS steels produced by SPS are typically 10–100 nm compared with <5 nm for HIPing under optimum conditions, and with a lower number density of 10^{19}–10^{21} m^{-3} compared with 10^{23} m^{-3} for HIPed materials [3,12]. However, SPS was still a relatively immature process for these alloys in these studies, and optimisation of SPS processing may be able to produce more desirable NCs < 5 nm diameter and with high number density $\sim 10^{23}$ m^{-3}, as described below.

Rajan et al. [24] studied the microstructure and hot hardness of ultrafine grained Fe–9Cr–1W + 0.5Y_2O_3 and Fe–9Cr–1Mo + 0.5Y_2O_3 based ferritic ODS alloys processed by MA and SPS. The addition of 0.25 wt% Ti enhanced the hardness at all temperatures from 298 to 973 K compared with the non-Y_2O_3 base alloy or Y_2O_3-containing alloy because of refined Ti–Y–O based NCs with a size range of

Table 1
Chemical compositions of Fe–14Cr pre-alloyed powder.

Element	Fe	Cr	Si	Mn	C	N	O
wt%	Bal	14.13	0.281	0.194	0.004	0.0095	0.052

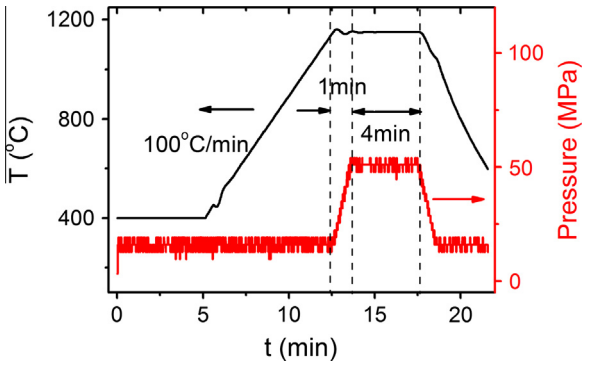

Fig. 1. The sintering temperature and pressure profiles for SPS consolidation of 14YT ODS alloys.

5–10 nm. Using TEM, APT and small angle neutron scattering (SANS), Heintze et al. [25] showed that nano-oxides in Fe–9Cr + 0.3Y_2O_3 and Fe–9Cr + 0.6Y_2O_3 materials fabricated by MA and SPS may still have refined radii of 2–15 nm and number density 1.4×10^{22} m^{-3} without the addition of Ti, while Park et al. [26] used TEM to resolve $YCrO_3$ with an average size of 10–20 nm in Fe–14Cr + 2Y_2O_3 steel fabricated by MA and SPS. Auger et al. [27] found 40–500 nm Cr-rich ($Cr_{23}C_6$ and Cr_2O_3) particles distributed along grain boundaries and small (12 ± 4 nm) Y-rich particles inside grains by TEM in Fe–14Cr + 0.3Y_2O_3 steels fabricated by MA and SPS. Compared with equivalent HIPed ODS steels, the SPS-processed counterparts exhibited lower yield and tensile strength from room temperature to 873 K, which was ascribed to more extensive intergranular decoration of Cr-rich particles and residual porosity.

Boulnat et al. [28,29] prepared Fe–14Cr–1W–0.3Ti + Y_2O_3 steels by MA and SPS and used SANS, which samples larger more representative volumes of material than either TEM or APT, to show NCs with a mean radius of 1.4 nm and number density of 1.4×10^{24} m^{-3}. When compared with HIP equivalents, these SPS alloys had a higher yield strength at room temperature and larger elongations at 600 °C, and similar yield strengths at 700 °C. The alloy had a bimodal grain size distribution that was suggested to arise from an initial, heterogeneous spatial distribution of stored energy from MA, leading to inhomogeneous recrystallization.

Bogachev et al. [30] studied the densification kinetics of MA Fe–13Cr–2Mo–0.3Y_2O_3 powder during SPS, reporting that a high heating rate (300–400 °C/min) was beneficial in achieving a final high density of bulk material. Rajan et al. [31] studied the effect of Y_2O_3 dispersoids on the sintering kinetics of Fe–9Cr–1Mo steel and suggested that the presence of nonconducting Y_2O_3 particles induced charge build up at the metal-dispersoid interfaces, and thus enhanced localised heat generation and mass transport. Ji et al. [32] attributed the development of a hetero-nanostructure containing nano (<100 nm), ultrafine (<500 nm) and micron-sized grains in MA and SPS Fe–39.78Al–0.054Zr–0.01B–0.2Y_2O_3 to temperature differences across the sample.

Summarising across these studies and recognising there remains some uncertainty in the densification mechanisms, SPS offers some promise for the rapid processing of ferritic steels containing oxide-based NCs, with indications that competitive microstructure and mechanical properties can be achieved. However there remains a lack of understanding on the precise nature of the critical NCs in SPS-processed ODS alloys and whether they are or are not essentially the same, or might be contrived to be the same, as those found in the more common HIP-processed alloys.

In this paper, we undertake a systematic investigation of the effect of SPS sintering temperature on the densification behaviour and microstructural evolution of an ODS ferritic steel prepared by MA. The Fe–14Cr–0.4Ti + 0.25Y_2O_3 (14YT) composition is chosen since this is a relatively simple system where the most comprehensive data is available in the literature. The microstructure, with a focus on NC evolution, is comprehensively characterised by means of scanning electron microscopy (SEM), electron backscatter diffraction (EBSD), transmission electron microscopy (TEM), scanning TEM (STEM) coupled with energy dispersive spectroscopy (EDS), and atom probe tomography (APT). We show that the densification of the 14YT alloy using SPS is significantly improved by increased sintering temperatures. Almost fully dense (99.6% of theoretical density) 14YT alloys could be successfully produced by SPS at 1150 °C with a pressure reduced from 200 to 50 MPa and process time reduced from 4 h to only 5 min. In addition to TEM and APT, synchrotron-based X-ray diffraction (XRD) is also used to provide complementary information on the crystal structure of the NCs from a comparatively large and more representative material volume. The presence of $Y_2Ti_2O_7$ NCs of the type found in HIP-processed materials is confirmed, with an average size of 3.5 nm and a number density of 1.04×10^{23} m^{-3}. A comparison and discussion of the limits of the various characterisation methods for NCs is also presented.

2. Experimental details

2.1. Powder processing by MA and SPS

Argon gas atomised Fe–14Cr pre-alloyed powders (<150 μm in diameter, Aubert & Duval, France), elemental Ti powder (<44 μm in diameter, 99.5%, Alfa Aesar, UK) and Y_2O_3 powder with a particle size ranging from 20 to 40 nm (Pi-Kem Ltd, UK) were used as starting materials for the MA Fe–14Cr–0.4Ti + 0.25Y_2O_3 (14YT) powder. The chemical composition of the Fe–14Cr pre-alloyed powders is given in Table 1. The powder mixture was mechanically alloyed in 99.999% purity Ar using a planetary mill (Pulverisette 6, Fritsch GmbH, Germany) with a chrome-steel bowl (500 ml) and AISI 52100 steel balls (800 g, 10 mm diameter) with a ball-to-powder weight ratio of 10:1 and a rotational speed of 150 rpm. A steady-state condition/microstructure of the 14YT powder was achieved after 60 h [33]. The 14YT powder was loaded into a graphite mould lined with graphite paper in an Ar-filled glove box for SPS consolidation. BN powder was sprayed on graphite paper in order to minimise carbon diffusion into the disc sample during sintering and to ease demolding after sintering. Then the mould and punches were sealed in a plastic bag and immediately transferred into the SPS furnace (FCT Systeme, Germany).

SPS consolidation was performed in a vacuum of 5–8 Pa at different temperatures ranging from 900 °C to 1150 °C, for 5 min under a peak uniaxial pressure of 50 MPa. In all cases the heating rate applied was 100 °C/min. The temperature was measured with an optical pyrometer focused on a central borehole in the upper punch close to the powder. During heating, a small pressure of 25 MPa was initially applied, sufficient to ensure particle–particle contact but insufficient to obtain consolidation that would inhibit degassing during heat up. Once the consolidation temperature was reached, the pressure was increased to 50 MPa within 1 min and then maintained constant until consolidation was finished. An example of the temperature (up to 1150 °C for consolidation) and pressure profiles for a typical SPS experiment is shown in Fig. 1. Since the minimum temperature that could be detected by the optical pyrometer was 400 °C, there is an apparent plateau temperature of ~400 °C at the beginning until the temperatures had risen sufficiently. After sintering, the power was switched off to allow the sample cool down to room temperature by direct contact with water-cooled punches. The dimension of the consolidated 14YT samples was typically 20 mm in diameter and 5 mm in thickness.

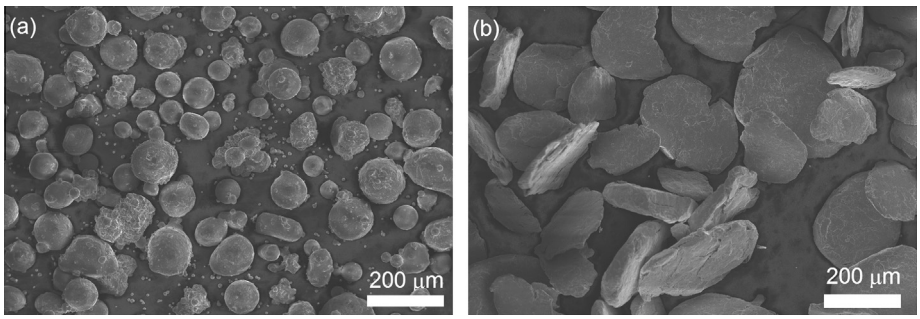

Fig. 2. SEM images of powder morphology: (a) Fe–14Cr pre-alloyed powder before MA, and (b) 14YT powder after MA.

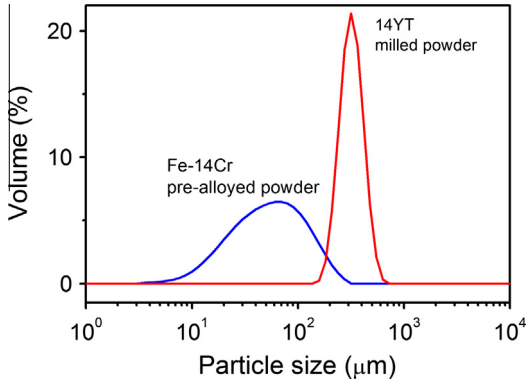

Fig. 3. Powder size distributions of Fe–14Cr pre-alloyed powder before MA and 14YT powder after MA.

2.2. Microstructural characterisation

The particle size distribution of pre-alloyed Fe–14Cr and milled 14YT powder was measured by laser diffraction (Mastersizer 2000, Malvern Instruments Ltd, UK). Consolidated 14YT discs were polished with SiC paper to remove surface contamination from the graphite die and foil and relative density measured by the Archimedes method in water. The morphology and microstructure of as-milled powder and bulk 14YT were observed by scanning electron microscopy (SEM; JEOL 840A). SPS samples for SEM observation were prepared by mechanical polishing and chemical etching in a 3:1:1 ratio of hydrochloric, nitric, and acetic acid. Electron backscatter diffraction (EBSD) was conducted in a JEOL JSM6500F operated at 20 keV and a probe current of ~10 nA; areas of ~80 × 108 μm^2 were mapped in a square array with a step size of 0.4 μm. The crystal structure of bulk 14YT was studied by high-resolution synchrotron X-ray diffractometry (XRD) at the Diamond Light Source (Didcot, UK) on beamline I11 with wavelength of 82.7136(2) pm.

TEM specimens were prepared by the "lift-out" technique using a Zeiss Auriga focused ion beam (FIB) system operating with 40 kV Ga ions, with the final milling stage carried out at 5 kV to avoid excessive Ga ion implantation. TEM studies used a JEOL2100 microscope operated at 200 kV or JEOL 3000F operated at 300 kV. A STEM with an annular dark field (ADF) detector was used for Z-contrast imaging, along with energy-dispersive X-ray spectroscopy to examine the chemical composition of particles. When determining the NC number density in ADF mode, the local foil thicknesses were measured by the convergent beam electron diffraction method.

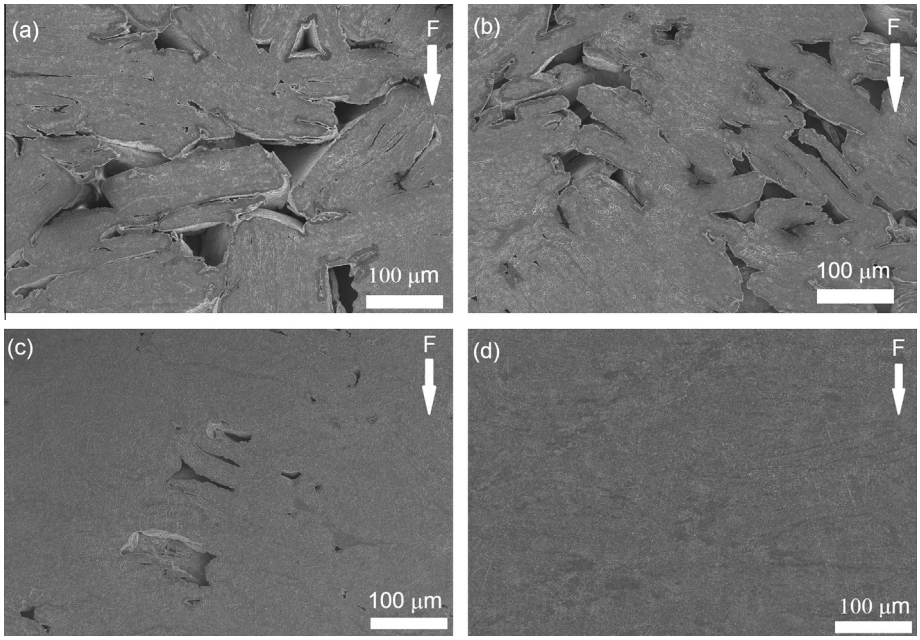

Fig. 4. SEM micrographs from polished and etched surface of bulk 14YT SPSed at different temperatures: (a) 900 °C, (b) 1000 °C, (c) 1100 °C, and (d) 1150 °C. The arrows indicate the direction of applied pressure.

To prepare APT samples from bulk 14YT, 0.5 × 0.5 × 10 mm rods were obtained by mechanical sectioning and then electropolished into sharply-pointed needles with an end radius of ~50 nm using a solution of 2% perchloric acid in 2-butoxyethanol. These specimens were then analysed in an Imago LEAP 3000HR instrument under laser pulsing mode (0.3–0.5 nJ energy, <10 μm beam spot size, 200 kHz repetition rate) at a specimen temperature of 30–50 K. 3D chemical maps with atomic spatial resolution were then reconstructed and cluster compositions were calculated from atoms selected using a method based on the maximum separation method. Core atoms of Y and O are selected using a maximum separation distance d_{max} = 1.3 nm. Clusters were defined as a group of at least N_{min} = 5 core atoms within distance d_{max}. The remaining atoms were included in a cluster if they were positioned within a surrounding distance L = 1.3 nm of a core atom defining the cluster. Once cluster atoms were isolated, the average cluster composition was calculated after using a local background subtraction in the mass spectrum and deconvoluting the overlapping mass-peaks of TiO^{++}/O_2^+ at 32 Da and TiO^+/Fe_2O^{++} at 64 Da. A standard error of 10% was assumed due to inaccuracies in mass-peak ranging and background subtraction, which was added to the statistical counting error for the number of atoms detected. 100 clusters were detected for assessment of the average cluster composition. An estimation of feature size was made from the radius of gyration (R_g), which is the average distance between each cluster atom and the centre of mass of the cluster. Further details of the determination of cluster compositions and size have been reported in previous publications [34,35].

3. Results and discussion

3.1. Powder morphology before and after MA

Fig. 2a shows that before MA, the gas atomised Fe–14Cr pre-alloyed powder had a typical spherical shape with a broad size distribution. During high-energy ball milling, the powder particles were repeatedly flattened, cold welded, fractured and re-welded, as shown in Fig. 2b. Fig. 3 shows pre-alloyed Fe–14Cr powder diameters from 5 to 305 μm with a mean of 69 μm. After milling, the distribution peak shifted towards larger diameters with a mean diameter according to laser diffraction of 316 μm, (but we note that this value will be distorted by the non-sphericity of the milled particles). There was also a much narrower distribution of apparent diameters in the milled powder, consistent with the SEM observations.

3.2. Effect of SPS sintering temperature on densification of 14YT alloys

Fig. 4 shows SEM micrographs from the polished and etched surface of 14YT alloys SPS sintered at different temperatures. At the lowest sintering temperature of 900 °C (Fig. 4a), the morphology of the as-milled flake powder was retained, with the short axes of the particles generally aligned along the direction of applied pressure (marked by an arrow in Fig. 4). There were both prior particle boundaries (PPBs) and large pores between particles, suggesting that only limited sintering had occurred. There was a dramatic reduction in both PPBs and pore fraction on sintering above 1000 °C (Fig. 4b and c). At 1150 °C, there was no resolvable porosity (Fig. 4d). When the temperature was increased further to 1180 °C, there was local melting indicating that we had reached the maximum process temperature for this powder.

The effect of sintering temperature on the relative density of 14YT is summarised in Fig. 5. The density at 1150 °C was 99.6%, similar to that found in ODS ferritic steels HIPed at 1100–1150 °C at 200 MPa for 4 h [15,16], confirming the potential advantage of SPS in requiring shorter dwell times and lower pressures. Applied pressure acts as an extra driving force for densification (alongside specific surface area reduction) and facilitates densification through particle sliding, oxide break-up and mechanical

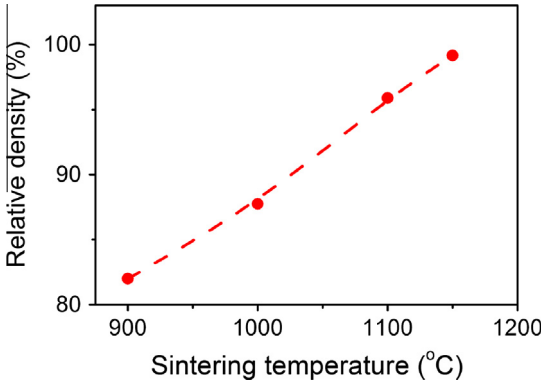

Fig. 5. Effect of sintering temperature on relative density of SPSed 14YT alloy.

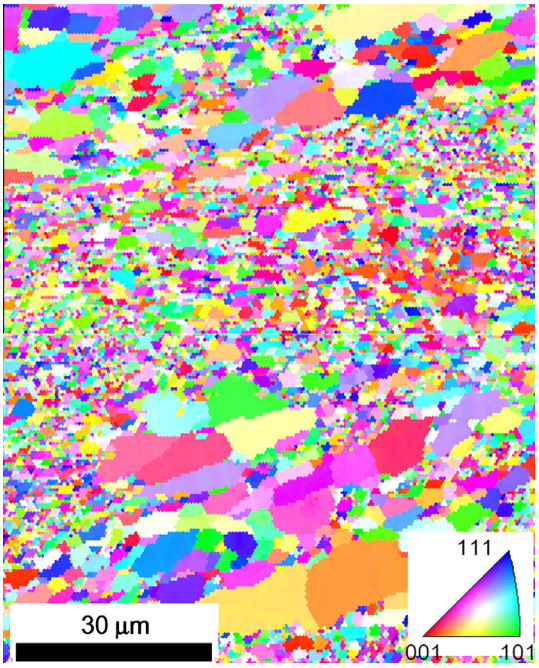

Fig. 6. EBSD orientation map of 14YT alloy SPSed at 1150 °C.

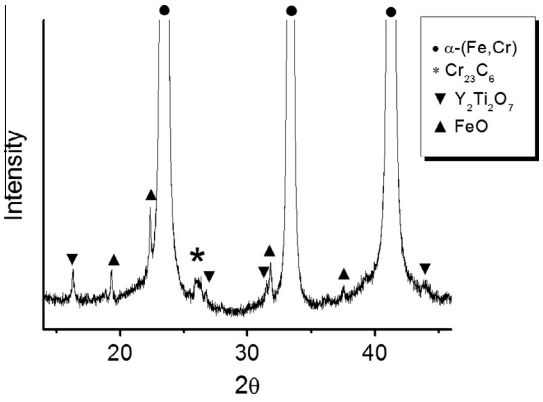

Fig. 7. Synchrotron XRD pattern of 14YT alloy SPSed at 1150 °C.

rearrangement, and plastic deformation. Moreover, particularly when electrically conductive metal materials are consolidated, non-thermal current effects may play a large role in the densification process, through enhanced (1) mass transport due to electromigration, which arises from momentum transfer by conduction electrons scattering from the activated metal ions in the solid and pushing these ions in the direction of the electron flow; (2) point defect generation, and (3) defect mobility [17].

3.3. Microstructure of 14YT alloys

Fig. 6 shows an EBSD image taken from 14YT SPSed at 1150 °C, with grain colours related to grain orientation expressed in the inset standard triangle. Grain boundaries having a misorientation >3° were identified as "high angle boundaries", and those with misorientation of 0–3° were identified as "sub-grain boundaries". The orientation imaging map indicated that grain orientation was essentially random, and the ferritic grain size distribution was bimodal, with peaks at 0.5 and 15 μm. Finer ferrite grains less than 500 nm in diameter could not be resolved. Similar bimodal grain size distributions have been reported for both HIPed and SPSed ferritic (>14% Cr) ODS steels [15,28]. This microstructure is usually ascribed to: (1) the formation of the larger ferrite grains by recovery and grain growth in regions with a lower density of nanoprecipitates due to inhomogeneities in the starting Y distribution [15,36]; and/or (2) incomplete recrystallization and abnormal grain growth in which a few large grains break away from pinning NCs and rapidly "consume" smaller, higher energy neighbours [37].

Fig. 7 shows a synchrotron XRD pattern from 14YT SPSed at 1150 °C. In addition to obvious peaks from the ferrite matrix, peaks due to $Y_2Ti_2O_7$ and FeO were resolved. Although there was only limited peak resolution of $Y_2Ti_2O_7$ in Fig. 7, these peaks could not be matched to any Y–Ti based oxide phases other than $Y_2Ti_2O_7$, which is the most stable of the Y–Ti oxide complexes. In addition, our results are in agreement with other studies [3,4]. The presence of a small volume fraction of FeO has also been reported for MA ODS steels [38,39]. A peak at $2\theta = 26^{o}$ was investigated against a large number of possible binary and mixed oxides or carbides, and showed closest matching to $Cr_{23}C_6$. Overall, all phases were consistent with those reported for similar alloys consolidated by HIP [40].

The different areas of foil specimens for TEM were examined in order to investigate the NC distribution. Fig. 8 shows a representative bright field (BF) TEM image obtained from 14YT SPSed at 1150 °C, with a high density of NCs homogeneously distributed in the matrix. Some NCs were clearly pinning dislocation lines. Fig. 9 shows a number of bright nanoparticles in a STEM image (boxed) and the associated EDS maps for Fe, Cr, Ti, Y and O. Qualitatively, the areas of Ti, Y and O enrichment coincided with Fe and Cr depletion, and supported identification of the NCs as being of the Y–Ti–O type. The contrast in STEM-ADF images is highly sensitive to local variations in the atomic number (Z-contrast images), which is a more suitable approach for detailed imaging of nano-sized, disperse oxide particles [7,41]. Fig. 10 is an ADF STEM image of the 14YT alloy after SPS at 1150 °C and suggested two possible sub-populations of NCs comprising cuboidal particles of 2–3 nm and spherical particles of 3–6 nm.

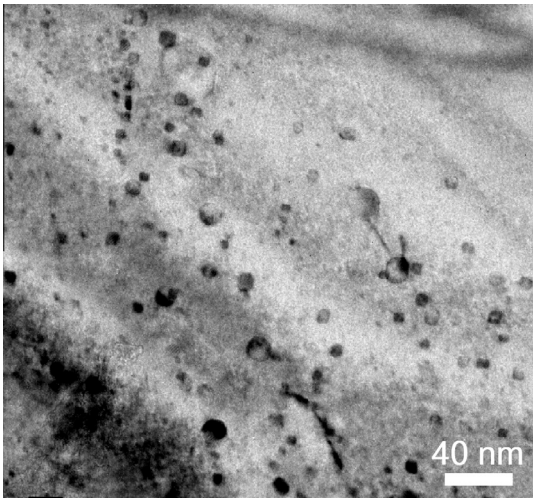

Fig. 8. Typical BF TEM micrograph of 14YT alloy SPSed at 1150 °C. The striations are associated with the FIB process used to section the specimens.

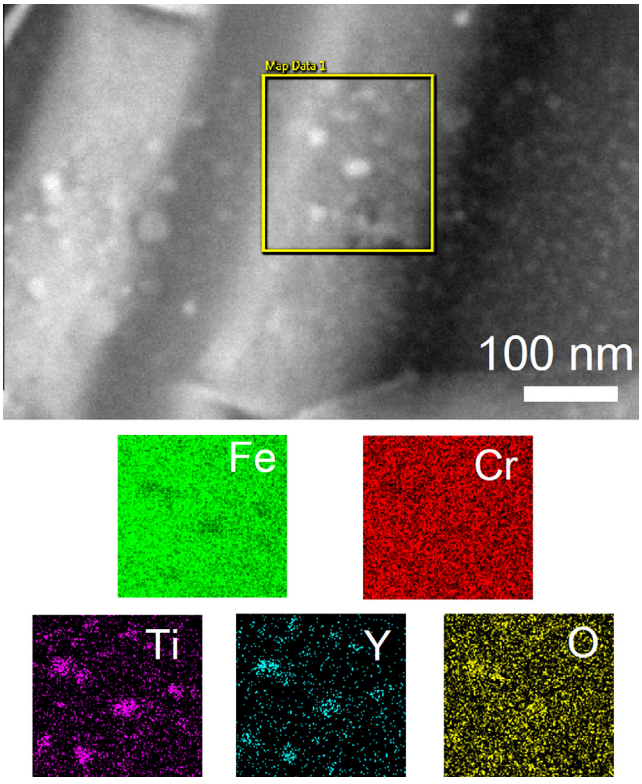

Fig. 9. STEM image and EDS mapping of 14YT alloy SPSed at 1150 °C.

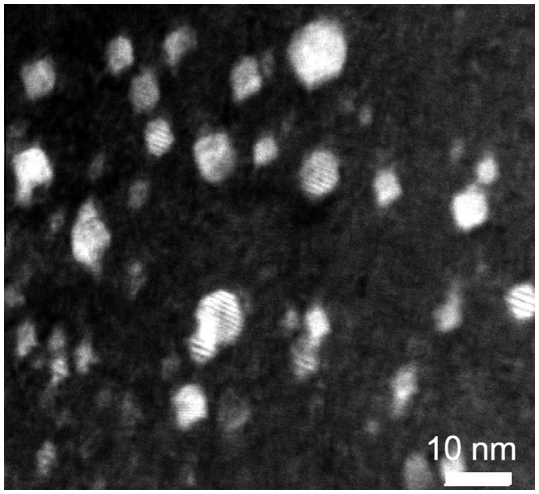

Fig. 10. ADF STEM image of 14YT alloy SPSed at 1150 °C.

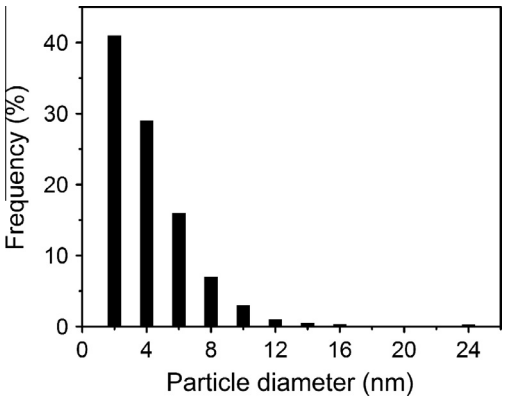

Fig. 11. Size distribution of NCs in 14YT alloy SPSed at 1150 °C.

A frequency plot of the NC diameter was determined by measuring 1339 particles from ADF STEM images obtained from different regions of several samples, and is shown in Fig. 11. The minimum and maximum NC diameter was 2.0 and 25 nm; the highest fraction of NCs was estimated at 42 ± 2.5% for NCs with diameters close to 2.0 nm, and overall the NC mean diameter and number density were 3.5 nm and 1.04×10^{23} m^{-3} respectively, which are consistent with those in similar MA-HIP alloys [12], although somewhat at the smaller diameter and higher fraction end of those reported.

APT element maps from 14YT sintered at 1150 °C are shown in Fig. 12a with Ti–Y–O rich NCs readily resolved. A number density of 1.4×10^{23} m^{-3} was estimated from the APT data, together with a average Guinier radius of 1.2 ± 0.4 nm, as shown in Fig. 12b. These values are consistent with TEM measurements, and those reported for HIP or extruded MA-based ODS alloys with the best mechanical performance in terms of tensile and creep strength

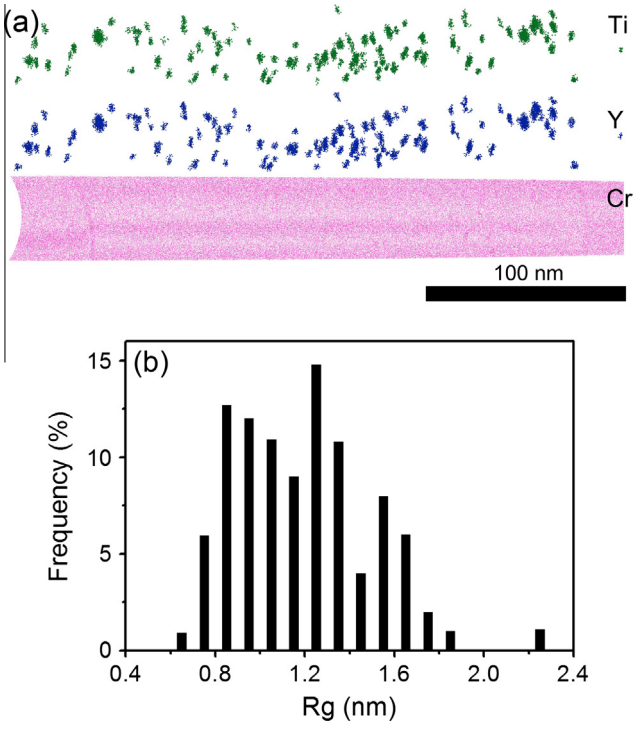

Fig. 12. APT results from 14YT alloy SPSed at 1150 °C: (a) 3D elemental maps in a region of high density of oxide particles; and (b) the size distribution of the Guinier radii of NCs from 14YT.

[1]. In general, all the microstructural data from SEM, TEM, XRD and APT indicate that high quality ODS alloys were successfully produced by SPS in the current work.

Composition line profiles obtained by averaging 100 clusters from APT reconstructed data is shown in Fig. 13, confirming the strong enrichment of Ti, Y, O and Cr in the NCs [42]. All the NCs had a similar chemical composition as shown in Table 2, with a Ti:Y atom ratio in the NCs of close to 1.0, which was consistent with $Y_2Ti_2O_7$.

Cr enrichment of the NCs (up to 33 at.%) in the corrected cluster composition obtained by APT apparently contradicts STEM–EDS results in Fig. 9, where Cr depletion of the NCs was suggested. However, discrepancies in NC structure and composition from TEM and APT have been previously reported [3,34,43–45] and have been explained by intrinsic instrument characteristics, creating measurement artefacts. The most significant effect leading to APT artefacts is the difference between the local evaporation fields and/or the electric fields at NC (insulating) and matrix (conducting) atoms, which causes differential evaporation and apparent Cr enrichment of the NCs [3,43]. The line profile (Fig. 13) indicates enrichment of Cr at the edges of the cluster more than the centre, as observed in other alloys [44]. In addition, APT is unable to sample reliably the largest NCs with relatively large spacing. TEM is able to characterise larger NCs from larger volumes, but conversely has restricted resolution of the smallest NCs, which can lead to lower NC number density estimates. In terms of the STEM EDS data from ⩽2 nm NCs embedded in the Fe-rich matrix, the NC signal is generally swamped by the matrix signal. Synchrotron XRD is able to sample the largest analysed volume and, providing minority phases are present in sufficient fraction, provides complementary and validating data for TEM and APT [46], as is the case in the present study.

The existence of Y–Ti–O NCs offer supports to the suggested mechanism that MA not only breaks up the Y_2O_3 particles, but dissociates them into yttrium and oxygen that is then dissolved into supersaturated solid solution in the ferrite matrix, to be re-precipitated in conjunction with dissolved Ti [6]. However, the incorporation of Ti into the NCs might also be conceived to occur during growth of very fine scale Y_2O_3, and dissolution of Y and O is not always reflected in the Fe lattice parameter changes that might be expected [13]. If dissolution of Y and O is occurring, it can be further conjectured that a single phase solid solution of Fe(Cr, Ti, Y, O) has a lower free energy at the milling temperature than a two phase mixture of a heavily defective matrix of Fe–14Cr–0.4Ti containing an increasingly fine dispersion of Y_2O_3. Even at the short timescales associated with heating in the SPS process, this highly defective solid solution is sufficiently unstable and the kinetics of NC nucleation and growth sufficiently are fast to

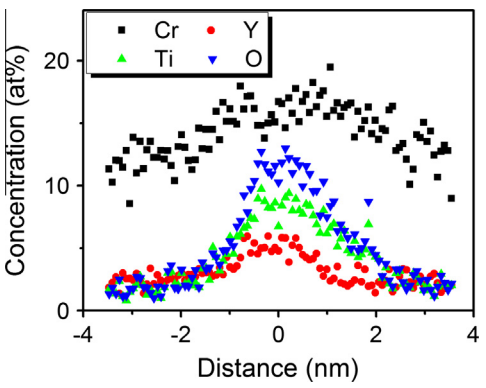

Fig. 13. Average composition line profiles of Ti–Y–O NCs determined by using APT analysis in the 14YT alloy SPSed at 1150 °C.

Table 2
NC composition in the 14YT alloys SPS-processes at 1150 °C and determined by APT analysis.

Element	Corrected cluster composition (at.%)
Cr	33 ± 3.6
Y	14 ± 1.7
Ti	13 ± 1.6
O	34 ± 3.8
Si	4.3 ± 0.6
C	1.3 ± 0.2
N	0.1 ± 0.0

form very similar NC distributions to those obtained in longer HIP cycles used more conventionally, alongside much accelerated movement of material to achieve near full density. The suggestion of two populations of closely related cuboidal and near spherical $Y_2Ti_2O_7$ particles may relate to very localised regions of increased Joule heating in the fast-consolidating powder mass that encourages some limited, localised coarsening of NCs.

4. Conclusions

The morphology and particle size distribution of spherical Fe–14Cr pre-alloyed powder were changed from near-spherical to a flattened, plate-like morphology with a narrower range of sizes after MA with 0.25 wt% Y_2O_3. During SPS, the relative density increased rapidly with sintering temperature, and 99.6% of theoretical density was achieved in only 5 min at 1150 °C and 50 MPa. The resulting ferrite grains had random orientation and a bimodal grain size distribution comprised of fine (<500 nm) and coarse grains (1–20 μm). Spherical and cuboidal $Y_2Ti_2O_7$ nanoclusters were dispersed in the ferritic matrix. The average size and number density of $Y_2Ti_2O_7$ NCs obtained from both STEM and APT investigations was <5 nm and of the order of 10^{23} m^{-3}, respectively. SPS is shown to produce high-density ODS ferritic alloys with a good dispersoid distribution at pressures and times significantly lower than those needed for consolidation by HIP. This shows its potential as a cost-effective approach for the consolidation of simple shapes from mechanically alloyed, high performance ODS steel powders.

Acknowledgements

This work was financially supported by the UK Engineering and Physical Sciences Research Council (EPSRC) under Grant EP/H018921/1. The authors would also like to thank the Diamond I11 beam line scientists Chiu Tang and Julia Parker, and further acknowledge financial support from EPSRC Grant EP/I012400/1 and Diamond proposal number 7528.

References

[1] G.R. Odette, M.J. Alinger, B.D. Wirth, Annu. Rev. Mater. Res. 38 (2008) 471–503.
[2] S. Ukai, M. Harada, H. Okada, M. Inoue, S. Nomura, S. Shikakura, K. Asabe, T. Nishida, M. Fujiwara, J. Nucl. Mater. 204 (1993) 65–73.
[3] Y. Wu, E.M. Haney, N.J. Cunningham, G.R. Odette, Acta Mater. 60 (2012) 3456–3468.
[4] H. Sakasegawa, L. Chaffron, F. Legendre, L. Boulanger, T. Cozzika, M. Brocq, Y. de Carlan, J. Nucl. Mater. 384 (2009) 115–118.
[5] D.J. Larson, P.J. Maziasz, I.S. Kim, K. Miyahara, Scripta Mater. 44 (2001) 359–364.
[6] M.K. Miller, D.T. Hoelzer, E.A. Kenik, K.F. Russell, J. Nucl. Mater. 329–333 (2004) 338–341.
[7] A. Hirata, T. Fujita, Y.R. Wen, J.H. Schneibel, C.T. Liu, M.W. Chen, Nature Mater. 10 (2011) 922–926.
[8] M.K. Miller, E.A. Kenik, K.F. Russell, L. Heatherly, D.T. Hoelzer, P.J. Maziasz, Mater. Sci. Eng. A 353 (2003) 140–145.
[9] M.K. Miller, D.T. Hoelzer, E.A. Kenik, K.F. Russell, Intermetallics 13 (2005) 387–392.
[10] T. Yamamoto, G.R. Odette, P. Miao, D.T. Hoelzer, J. Bentley, N. Hashimoto, H. Tanigawa, R.J. Kurtz, J. Nucl. Mater. 367–370 (2007) 399–410.
[11] P. Pareige, M.K. Miller, R.E. Stoller, D.T. Hoelzer, E. Cadel, B. Radiguet, J. Nucl. Mater. 360 (2007) 136–142.
[12] M.J. Alinger, G.R. Odette, D.T. Hoelzer, Acta Mater. 57 (2009) 392–406.
[13] I. Hilger, M. Tegel, M.J. Gorley, P.S. Grant, T. Weißgärber, B. Kieback, J. Nucl. Mater. 447 (2014) 242–247.
[14] L.L. Hsiung, M.J. Fluss, S.J. Tumey, B.W. Choi, Y. Serruys, F. Willaime, A. Kimura, Phys. Rev. B 82 (2010) 184103.
[15] P. Miao, G.R. Odette, T. Yamamoto, M. Alinger, D. Hoelzer, D. Gragg, J. Nucl. Mater. 367–370 (2007) 208–212.
[16] Z. Oksiuta, N. Baluc, Nucl. Fusion. 49 (2009) 055003.
[17] Z.A. Munir, D.V. Quach, J. Am. Ceram. Soc. 94 (2011) 1–19.
[18] Cs. Balázsi, F. Gillemot, M. Horváth, F. Wéber, K. Balázsi, F.C. Sahin, Y. Onüralp, Á. Horváth, J. Mater. Sci. 46 (2011) 4598–4605.
[19] S.K. Karak, J.D. Majumdar, W. Lojkowski, A. Michalski, L. Ciupinski, K.J. Kurzydlowski, I. Manna, Phil. Mag. 92 (2012) 516–534.
[20] Q.X. Sun, T. Zhang, X.P. Wang, Q.F. Fang, T. Hao, C.S. Liu, J. Nucl. Mater. 424 (2012) 279–284.
[21] Q.X. Sun, Y. Zhou, Q.F. Fang, R. Gao, T. Zhang, X.P. Wang, J. Alloys. Compd. 598 (2014) 243–247.
[22] Y.P. Xia, X.P. Wang, Z. Zhuang, Q.X. Sun, T. Zhang, Q.F. Fang, T. Hao, C.S. Liu, J. Nucl. Mater. 432 (2013) 198–204.
[23] R. Gao, T. Zhang, X.P. Wang, Q.F. Fang, C.S. Liu, J. Nucl. Mater. 444 (2014) 462–468.
[24] K. Rajan, V.S. Sarma, T.R.G. Kutty, B.S. Murty, Mater. Sci. Eng. A 558 (2012) 492–496.
[25] C. Heintze, M. Hernández-Mayoral, A. Ulbricht, F. Bergner, A. Shariq, T. Weissgärber, H. Frielinghaus, J. Nucl. Mater. 428 (2012) 139–146.
[26] J.J. Park, S.M. Hong, E.K. Park, M.K. Lee, C.K. Rhee, J. Nucl. Mater 428 (2012) 35–39.
[27] M.A. Auger, V. Castro, A. Muñoz, R. Pareja, J. Nucl. Mater. 436 (2013) 68–75.
[28] X. Boulnat, D. Fabregue, M. Perez, M. Mathon, Y. Decarlan, Metall. Mater. Trans. 44A (2013) 2461–2465.
[29] X. Boulnat, M. Perez, D. Fabregue, T. Douillard, M. Mathon, Y. Decarlan, Metall. Mater. Trans. 45A (2014) 1485–1497.
[30] I. Bogachev, E. Grigoryev, O.L. Khasanov, E. Olevesky, JOM 66 (2014) 1020–1026.
[31] K. Rajan, T. Shanmugasundaram, V.S. Sarma, B.S. Murty, Metall. Mater. Trans. 44A (2013) 4037–4041.
[32] G. Ji, F. Bernard, S. Launois, T. Grosdidier, Mater. Sci. Eng. A 559 (2013) 566–573.
[33] H. Zhang, M.J. Gorley, K.B. Chong, M.E. Fitzpatrick, S.G. Roberts, P.S. Grant, J. Alloy. Compd. 582 (2014) 769–773.
[34] C.A. Williams, E.A. Marquis, A. Cerezo, G.D.W. Smith, J. Nucl. Mater. 400 (2010) 37–45.
[35] C.A. Williams, P. Unifantowicz, N. Baluc, G.D.W. Smith, E.A. Marquis, Acta Mater. 61 (2013) 2219–2235.
[36] H. Kishimoto, M.J. Alinger, G.R. Odette, T. Yamamoto, J. Nucl. Mater. 329–333 (2004) 369–371.
[37] P. He, M. Klimenkov, R. Lindau, A. Möslang, J. Nucl. Mater. 428 (2012) 131–138.
[38] R. Vijay, M. Nagini, J. Joardar, M. Ramakrishna, A.V. Reddy, G. Sundararajan, Metallurgical Mater. Trans. A 44 (2013) 1611–1620.
[39] A.V. Litvinov, V.A. Shabashov, K.A. Kozlov, N.F. Vil'danova, V.V. Sagaradze, Inorgan. Mater. 45 (2009) 1018–1025.
[40] R. Schaeublin, T. Leguey, P. Spätig, N. Baluc, M. Victoria, J. Nucl. Mater. 307–311 (2002) 778–782.
[41] A. Hirata, T. Fujita, C.T. Liu, M.W. Chen, Acta Mater. 60 (2012) 5686–5696.
[42] A.J. London, S. Lozano-Perez, M.P. Moody, S. Amirthapandian, B.K. Panigrahi, C.S. Sundar, C.R.M. Grovenor, Ultramicroscopy 2015, in press. doi: 10.1016/j.ultramic.2015.02.013.
[43] N. Cunningham, Y. Wu, D. Klingensmith, G.R. Odette, Mater. Sci. Eng. A 613 (2014) 296–305.
[44] E.A. Marquis, Appl. Phys. Lett. 93 (2008) 181904.
[45] S. Lozano-Perez, V.C. Bernal, R.J. Nicholls, Ultramicroscopy 109 (2009) 1217–1228.
[46] J.-L. Béchade, D. Menut, M.-L. Lescoat, B. Sitaud, S. Schlutig, P.L. Solari, I. Llorens, H. Hermange, Y. de Carlan, J. Ribis, L. Toualbi, J. Nucl. Mater. 428 (2012) 183–191.